Title

Liquefaction of granular materials in constant-volume cyclic shearing: Transition between solid-like and fluid-like states

Authors

Yang, Ming
Taiebat, Mahdi
Radjai, Farhang

Publication Date

2022-08-01

DOI

10.1016/j.compgeo.2022.104800

Peer reviewed

Computers and Geotechnics 148 (2022) 104800

Contents lists available at ScienceDirect

Computers and Geotechnics

journal homepage: www.elsevier.com/locate/compgeo

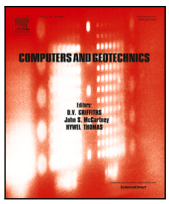

Research paper

Liquefaction of granular materials in constant-volume cyclic shearing: Transition between solid-like and fluid-like states

Ming Yang [a,b], Mahdi Taiebat [b,*], Farhang Radjaï [c]

[a] Department of Civil and Environmental Engineering, Northwestern University, Evanston, IL, USA
[b] Department of Civil Engineering, University of British Columbia, Vancouver, BC, Canada
[c] CNRS, Laboratoire de Mécanique et Génie Civil, University of Montpellier, Montpellier, France

ARTICLE INFO

Keywords:
3D-DEM
Granular media
Cyclic liquefaction
Micro and meso-scale study

ABSTRACT

By means of 3D-DEM cyclic simple shear simulations at constant volume, this paper analyzes the evolution of the internal structure during cyclic liquefaction of dense granular media. Upon liquefaction, the granular system undergoes a fast transition to a regime where the fluid-like shear strain develops. This regime is characterized by low shear modulus, decreasing dilatancy, and reduced shear viscosity. We analyze the internal structure by means of several micro- and meso-scale descriptors, including coordination number, fabric anisotropy, number of clusters, a fraction of maximum cluster size, and a percolation index. We select a typical post-liquefaction cycle in which we highlight several particular states that naturally divide the cycle into different periods. During liquefaction, the system deforms significantly with an enhanced number of binary collisions initially and particle clusters subsequently. Both the coordination number and percolation index increase while fabric anisotropy oscillates. The fluid-like to solid-like transition is characterized by a well-defined value of the coordination number (3.6) when the particles percolate across the system. From the analysis of the micro- and meso-scale behaviors, we further discuss two possible criteria for exiting the fluid-like state based on the excess pore pressure.

1. Introduction

The cyclic liquefaction of saturated soils is a topic of paramount importance because of its widespread engineering applications. It usually occurs in response to sustained cyclic shearing of small amplitude and transitions to a fluid-like state with catastrophic loss of shear strength and large irreversible strains (Castro, 1975; Ishihara, 1993). Conventional triaxial or simple shear tests on either constant-volume or saturated undrained condition of soil samples have been performed to study these phenomena, inducing extensive investigation on the liquefaction triggering (Ishihara, 1993; Wu et al., 2004; Kokusho, 2013), effects of initial and loading conditions on liquefaction resistance (Vaid and Sivathayalan, 1996; Yang and Sze, 2011; Vargas et al., 2020), and reliquefaction (Yamada et al., 2010; Fardad Amini et al., 2021), among others. As most conventional laboratory studies only involve the measurements of stresses and strains at the sample scale, the liquefaction induced by cyclic shearing is inferred from these macroscopic quantities.

Obviously, the liquefaction behavior as modeled from the measured variables at the sample scale reflects the internal structure at the micro and meso scales. There is a growing interest in the micromechanics of granular materials, mostly from the grain-scale approach, for a better understanding of the soil response. It has the potential to found the soil behavior on fundamental research by deriving coarse-grained laws from the collective behavior of grains (Radjaï et al., 2017). This renewed interest in micromechanics is not just a luxury; it reflects a real need for enhanced understanding and predictive modeling of soils (Mitchell et al., 2005). The micromechanical approach can provide valuable insights and physical grounds for developing physics-based constitutive models. Undrained cyclic shearing of isotropically consolidated sand is an example of complex behaviors that leads to degradation of mean effective stress. In particular, each loading reversal following a dilative phase involves a large amount of contraction that significantly reduces the mean effective stress (Ishihara et al., 1975). Several constitutive models are proposed to reproduce this phenomenon by properly formulating the dilatancy (e.g., Papadimitriou et al., 2001; Dafalias and Manzari, 2004; Zhang and Wang, 2012; Tasiopoulou and Gerolymos, 2016; Liao and Yang, 2021). However, the micromechanical origins of this phenomenon and thus the validity of the mechanisms considered in constitutive models have so far remained unexplored. In addition, cyclic liquefaction usually occurs at very small mean effective stress

* Corresponding author.
E-mail address: mtaiebat@civil.ubc.ca (M. Taiebat).

https://doi.org/10.1016/j.compgeo.2022.104800
Received 29 November 2021; Received in revised form 24 March 2022; Accepted 26 April 2022

and with significant shear strain accumulation. The constitutive models that can simulate such large deformations in the plasticity framework assume that significant plastic shear strains occur when the mean effective stress is low and thus shear stiffness is small (Elgamal et al., 2003; Wang et al., 2014; Barrero et al., 2020; Yang et al., 2022a; Liao and Yang, 2021). Although this approach has met particular success, there remain open questions regarding the quantitative description of the transition between solid-like and fluid-like states and the effective viscosity of the liquefied state.

Answering these questions needs a detailed investigation of the evolution of granular microstructure under cyclic shearing. Some special experimental techniques have been used in cyclic shearing, such as scanning electronic microscopy (Ni et al., 2021), to correlate the initial fabric to liquefaction resistance. However, the insight gained from laboratory studies can be significantly enhanced by using the widely adopted numerical approach of discrete element method (DEM). The particle dynamics DEM (Cundall and Strack, 1979) simulates motions of the particles by accounting for frictional contact interactions between particles (Radjaï and Dubois, 2011), allowing thereby the investigation of the mechanical response of granular materials from both macroscopic and grain-scale perspectives. Its application to cyclic liquefaction dates back to Ng and Dobry (1994). Several subsequent DEM studies have revealed that cyclic liquefaction is accompanied by a sudden falloff of the coordination number (Sitharam, 2003; Wang and Wei, 2016; Wei et al., 2018; Barrero et al., 2018) and the so-called redundancy index (Huang et al., 2018; Martin et al., 2020), large rearrangements of granular fabric (Huang et al., 2018; Yang et al., 2021; Rahman et al., 2021), a fragile force network (Wei et al., 2018; Huang et al., 2019a; Yang et al., 2021) and a rolling contact fraction exceeding the sliding contact fraction (Gu et al., 2020). Some other studies (Huang et al., 2019b; Martin et al., 2020) have focussed on the mesoscale structures such as loop-like clusters encompassed by contacts, leading to the observation that the largest particle cluster declines in both size and dimensions in the liquefaction state.

Most DEM studies of liquefaction mainly focus on the process of entering the liquefaction state, i.e., the transition from a solid-like state to a fluid-like state. This transition during cyclic shearing occurs instantaneously. Before entering the liquefaction state, most contacts in the granular system are lost, and the contact network collapses, thereby inducing large fluctuations of the internal structure. Because of the abrupt nature of these changes, the transition from the solid-like state to the fluid-like state is not well defined from the viewpoint of the microscale and mesoscale descriptors (Yang et al., 2021). An alternative approach, for not very loose samples, consists in assessing the exit from the fluid-like state in cyclic shearing, i.e., the transition from the fluid-like state back to the solid-like state. Some recent studies (Wei et al., 2018; Huang et al., 2019a,b; Yang et al., 2021) have analyzed the reconstruction of the internal structure of the liquefied granular system from the microscale and mesoscale descriptors. For example, in a two-dimensional (2D) DEM study, Wei et al. (2018) pointed out a critical coordination number value of 2.0 as the transition point between flow state and hardening state under shearing and suggested a unique hardening state line defined by void-based fabric anisotropies. But the link between these variables and the macroscopic behavior requires further investigation.

In this paper, we use three-dimensional (3D) DEM simulations to perform constant-volume cyclic simple shearing of granular materials with the goal of obtaining a quantitative description of microstructural evolution during cyclic liquefaction and its correlation with macroscopic variables. Samples of spherical particles are prepared under isotropic compression and then cyclically sheared for a long time both in pre-liquefaction and post-liquefaction periods. We first present the details of sample preparation and simulation protocols. Then, we analyze the transition between the solid-like and the fluid-like states from the macroscopic perspective. The internal structure evolution is then explored via several microscale and mesoscale descriptors to highlight the transition between the fluid-like and the solid-like states. Finally, we discuss the mechanisms underlying a stress-based criterion for exiting the fluid-like state.

2. Numerical procedure

An in-house 3D particle dynamics DEM program, named GRFlow3D (Mutabaruka, 2013), is used in this work. The granular system is simulated using spheres interacting via soft-contact laws. The contact interactions between spheres consist of normal collision, tangential sliding, rolling, and torsion. The key quantity is the elastic deflection between particles, from which the corresponding normal force is determined using a linear spring–dashpot model. The simulation involves two stages: (1) building a particle assembly via isotropic compression and (2) applying cyclic simple shearing to the assembly under constant volume conditions.

The sample consists of 8000 spherical particles with weak polydispersity, i.e., $d_{\max}/d_{\min} = 2$ where $d_{\min} = 1$ mm and $d_{\max}$ refer to the minimum and maximum particle diameters, respectively. Between $d_{\min}$ and $d_{\max}$, the particle size follows a uniform distribution of particle volumes, thus the number of particles belonging to a size class of diameter d is proportional to d^{-3} (Mutabaruka et al., 2019). When the particles are generated, they are placed randomly on a three-dimensional (3D) sparse lattice to avoid overlap. This 3D lattice is contained in a rectangular biperiodic cell whose top and bottom sides are rigid walls, and four lateral sides are periodic boundaries. Then, the sample is compressed isotropically by translating the six sides of the cell. The gravity is set to zero. The tangential friction coefficient μ_t is tuned to prepare a sample with a targeted void ratio e and then is set to 0.5 in the subsequent shearing process. A simple computational procedure modified from Thornton (Thornton, 2015) is adopted to prepare samples comparable with those in experiments, as detailed in Yang et al. (2021). Following this procedure, setting $\mu_t = 0$ and 0.5 will lead to samples with void ratios of 0.561 and 0.725, respectively, usually deemed close to the lowest accessible void ratio $e_{\min}$ and the largest accessible void ratio $e_{\max}$ (Kuhn et al., 2014). Fig. 1(a) displays an isotropically compressed sample with $e = 0.626$ or relative density $D_r \simeq 59$ % under a mean pressure $p_0 = 100$ kPa.

During cyclic shearing, the sample volume is maintained constant by fixing four lateral sides and the bottom wall while keeping the sample height constant. Cyclic simple shearing is imposed by moving the top wall horizontally at a constant velocity v_x along the x axis (see Fig. 1(b)). This numerical setting with periodic lateral side boundaries is different from the Cambridge- or NGI-type simple shear devices; here the lateral sides of the sample are not rotated by horizontal movement of the top wall. To eliminate slippage between the walls and the sample, a layer of particles is glued to the top and bottom walls as indicated by the dark gray spheres in Fig. 1(b). The shear direction is reversed each time the magnitude of shear stress τ, extracted from the calculated stress tensor (see below), reaches a target amplitude τ^{amp}. The total strain needed to reach this amplitude is not constant and depends on the state of liquefaction, as we shall see below.

To choose the shear rate, we consider the inertial number $I = \dot{\gamma}\bar{d}\sqrt{\rho/p}$, where $\dot{\gamma} = |v_x|/h$ is the shear strain rate with h the sample height, ρ the solid density of the particles, and $\bar{d}$ the mean particle diameter. The inertial number represents the shear rate normalized by the relaxation rate under the action of the average pressure p. The shear is practically quasistatic if $I < 10^{-3}$ (MiDi, 2004). During constant-volume cyclic shearing, I varies due to the changes of p. When the sample liquefies, p degrades to vanishingly small values due to unjamming, and hence I may increase beyond 10^{-3} whatever its value before unjamming. In this study, we set $v_x = 0.01$ m/s so that $\dot{\gamma} \simeq 0.38$ s^{-1}, which is consistent with Martin et al. (2020). For this choice, the simulation is faster while shearing is quasistatic during jammed (solid-like) states. The higher values of I at unjamming occur as a result of unstable deformation and sudden decrease of p, which is an intrinsic feature of cyclic liquefaction only and not influenced by the loading rate.

The simulation parameters are given in Table 1. The rolling and torsion stiffness and friction coefficients are set to small nonzero values in order to make the rotations slightly dissipative as a simple way to account for the effects due to aspherical particle shape or surface roughness (Radjaï and Dubois, 2011).

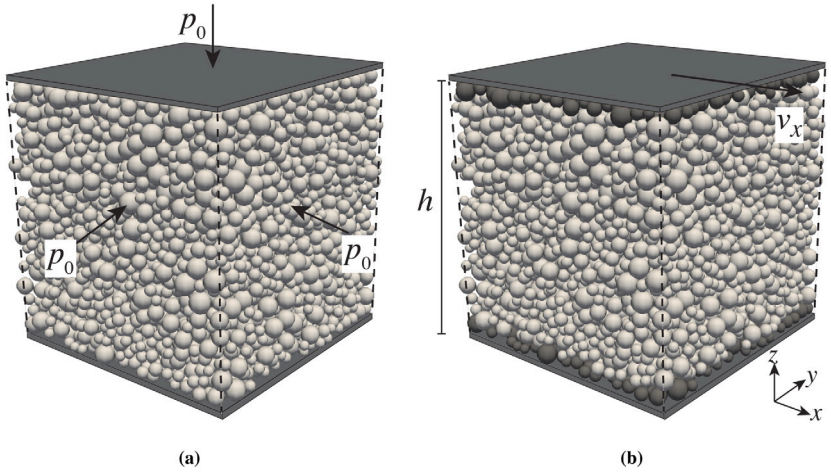

Fig. 1. Illustration of particle arrangements and boundary conditions for a sample composed of 8000 particles: (a) at the end of sample preparation; (b) during constant-height cyclic shearing. The dark gray particles in (b) are glued to the top and bottom walls of the simulation cell.

Table 1
DEM parameters.

Description	Value
Particle density, ρ	2650 kg/m^3
Normal stiffness, k_n	10^6 N/m
Normal viscosity, c_n	1.15 kg/s
Tangential stiffness, k_t	$0.8k_n$
Tangential viscosity, c_t	$0.2c_n$
Tangential friction coefficient, μ_t	0.5
Rolling stiffness, k_r	$0.1k_n$
Rolling viscosity, c_r	$0.05c_n$
Rolling friction coefficient, μ_r	0.1
Torsion stiffness, k_o	$0.1k_n$
Torsion viscosity, c_o	$0.05c_n$
Torsion friction coefficient, μ_o	0.1

3. Macroscopic response

The stress tensor $\boldsymbol{\sigma}$ of the granular packing is determined from the contact forces and particle positions over a selected volume V:

$$\boldsymbol{\sigma} = \frac{1}{V} \sum_{c \in N_c} \boldsymbol{l}^c \otimes \boldsymbol{f}^c \tag{1}$$

where $\boldsymbol{l}^c$ is the branch vector connecting the centers of two particles for interior contact or connecting the particle center and the contact point for exterior contact, $\boldsymbol{f}^c$ is the contact force, $\otimes$ denotes the dyadic tensor product, and the summation runs over all the contacts N_c belonging to V. In the simple shear test, the shear stress τ and mean effective stress p are given by $\tau = \tau_{zx}$ and $p = (\sigma_{xx} + \sigma_{yy} + \sigma_{zz})/3$, respectively.

Although pore water is not explicitly incorporated in these DEM simulations, the excess pore pressure in the equivalent truly undrained system can be deduced from the variation $\Delta u = p_0 - p$ of the pore pressure, which is simply the amount of load not supported by the particles and therefore supported by the saturating fluid. The excess pore pressure ratio is given by $r_u = \Delta u/p_0 = 1 - p/p_0$. The shear strain γ is the ratio x_w/h, where x_w is the cumulative horizontal displacement of the top wall. The number of cycles N is used as a time variable instead of running time t, where a fractional cycle number is defined by interpolation between two successive cycles. A cycle starts with $\gamma = 0$, approaches a quarter when γ reaches the positive amplitude, becomes a half when γ drops back to zero, and attains the third quarter with negative value of γ.

Fig. 2 displays the simulated macroscopic response of a dense sample subjected to constant-volume cyclic simple shearing, including the stress path of shear stress τ versus mean effective stress p, and the shear stress–strain curves. The simulation starts from $p = 100$ kPa, $\tau = 0$ kPa, and $\gamma = 0$. As τ oscillates between $-\tau^{\text{amp}}$ and τ^{amp}, p declines at an increasing rate and then decreases significantly upon reverse loading after a dilative phase (p increasing) while the shear strain develops at the same time. When p drops below 1 kPa or r_u exceeds 0.99, the system is deemed liquefying or staying in the fluid-like state (Shamoto et al., 1997) and this threshold is considered to be a simple and practical liquefaction criterion (Ishihara, 1993). The first time that r_u reaches 0.99 is named 'initial liquefaction', and the shear process before and after this point are referred to as pre- and post-liquefaction periods, respectively. In the post-liquefaction period, the stress path gets trapped in a typical 'butterfly' shape and the corresponding stress–strain loops keep expanding at each cycle — a manifestation of the so-called 'cyclic mobility'.

A post-liquefaction loading cycle, named cycle C, is highlighted in Fig. 2, where the stress path follows the 'butterfly' shape and γ oscillates at an amplitude of $\simeq 3\%$. To explore this post-liquefaction cycle, several particular states are selected to divide this cycle into smaller intervals. In particular, S_1 refers to the state with $\tau = -\tau^{\text{amp}}$; S_2 refers to the state when τ changes its sign from negative to positive; S_3 is defined as the state when p approaches its local minimum $p_{\min}$, after which p starts to increase, corresponding to the phase transformation (PT) point; S_4 is the state when p increases to 1 kPa (or r_u decreases back to 0.99), i.e., the practical stress-based criterion for exiting the fluid-like state. S_5, S_6, S_7, and S_8 are similar to S_1, S_2, S_3, and S_4, respectively, but in the other half of the selected cycle. The state S_9 ends this shearing cycle. It should be noted that we do not mark the state representing the entrance in the fluid-like state (i.e., r_u increasing to 0.99), which occurs between S_1 and S_2 or S_5 and S_6. This is because upon reverse shearing from S_1 or S_5, the initially well-connected contact network 'instantaneously' breaks down at such a level of r_u, inducing network collapse prior to the fluid-like state. The corresponding state for $r_u = 0.99$ is very close to S_2 or S_6.

Fig. 2(b) shows that most of the shear strain happens in the fluid-like state (between S_2 and S_4 or S_6 and S_8), which is referred to as 'fluid-like shear strain' (Shamoto et al., 1997). This observation is consistent with laboratory findings and provides here a basis for mechanics-based modeling of post-liquefaction shear strain (Elgamal et al., 2003; Zhang and Wang, 2012; Barrero et al., 2020). For example, Elgamal et al. (2003) proposed that at low confinement levels near liquefaction, a constant-volume perfectly plastic phase to be activated and the stress state remains at PT (S_3 or S_7), until a user-defined octahedral shear strain increment is accumulated. However, Fig. 2(b) indicates that the majority of the fluid-like shear strain is not developed at PT but between S_3 and S_4 or between S_7 and S_8, namely after PT and while p remains quite low. Our finding also contradicts Shamoto et al. (1997)

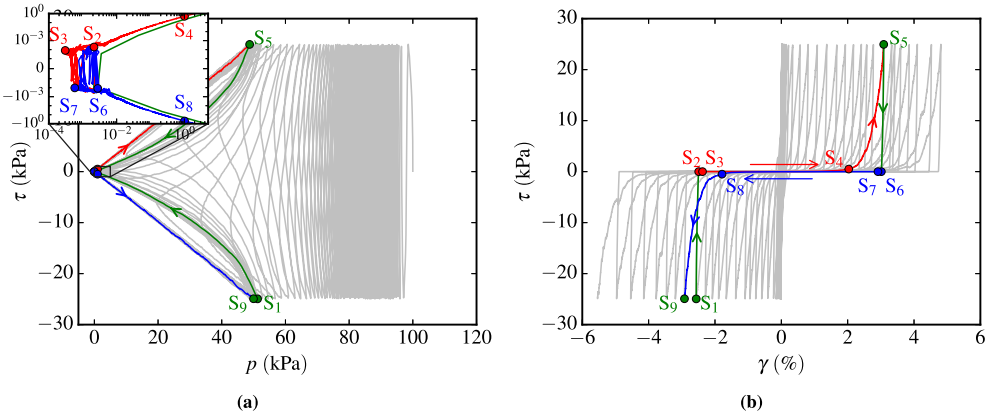

Fig. 2. Macroscopic response of a constant-volume cyclic simple shear test on a dense sample for $e = 0.626$ and $p_0 = 100$ kPa: (a) stress path; (b) stress–strain response. The highlighted post-liquefaction cycle is named cycle C.

and Zhang and Wang (2012) who assumed the development of fluid-like shear strain at zero effective confining stress as the inset window of Fig. 2(a) does not show the existence of zero p. In fact, the granular system does go through a collisional phase with a fragile contact network but does not completely lose its strength (Ishihara, 1993), as reflected also by the chaotic stress path in the inset window. We adopt S_4 or S_8 (corresponding to $r_u = 0.99$) roughly as the exit criterion from this chaotic region, implying the regain of a stable contact network. One may question this choice for exiting the fluid-like state given that the inset window of Fig. 2(a) does not seem to correspond to anything critical near S_4 or S_8. While this looks to be the case in the macroscopic response, we will return to this point when we present the simulation data on the internal structure evolution of the granular system in the liquefaction region.

It is recognized that a granular system transitions from solid-like to fluid-like behavior once it liquefies by developing a rapid and significant accumulation of shear strain with minimal change in the stress state. It is not clear whether at this state the system flows like a fluid sustaining no shear stress in the limit of vanishing shear rate, namely 'zero-stress flow' (Heussinger and Barrat, 2009), or it still presents a finite shear stress value ('yield-stress flow') but not large enough to maintain a jammed state. One should not confuse 'yield-stress flow' here with 'hardening state' described in some previous studies (Shamoto et al., 1997; Zhang and Wang, 2012; Wei et al., 2018) since the latter refers to solid-like states. In our nearly quasi-static simulations, the evolution of τ and p in the post-liquefaction cycle C is presented in Fig. 3, with the interesting region near S_2 highlighted in the inset. Consistently with the inset to Fig. 2(a), p does not vanish thoroughly. Between S_2 and S_3, τ fluctuates mildly around zero, implying the alternate appearance of zero-stress flow and yield-stress flow. This alternating behavior disappears after S_3 as τ starts then to increase steadily. One can thus conclude that the yield-stress flow rather than the zero-stress flow dominates in liquefaction, producing most of the shear strain that is developed.

In each post-liquefaction cycle, p tends to zero in the fluid-like state, with its lowest value denoted by $p_{\min}$. Fig. 4 displays the variation of $p_{\min}$ reached in post-liquefaction period for cyclic shear simulations of three samples with different values of the void ratio 'cyclic stress ratio' CSR = 0.25, defined as the ratio τ^{amp}/p_0. We see that the looser samples show slightly lower values of $p_{\min}$, and p never vanishes. For the three samples, $p_{\min}$ decreases during the first several cycles of the post-liquefaction period, but then it nearly levels off.

Regarding the state change of the granular system approaching a fluid-like state, one may question its rate-dependent nature. Some laboratory experiments (Hwang et al., 2006; Chen et al., 2013, 2016) have studied the fluid characteristics of liquefying sand and identified it as a shear-thinning non-Newtonian fluid characterized by a decreasing

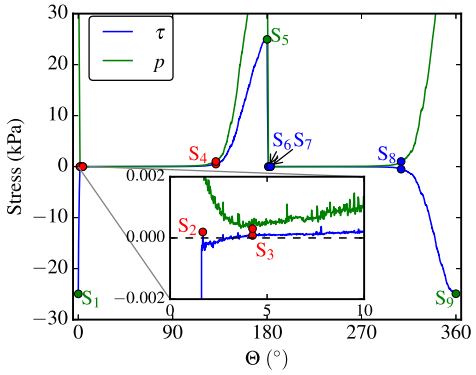

Fig. 3. Evolution of shear stress and mean effective stress in cycle C as a function of normalized time $\Theta = 360t/T$ where T is the time period of the shear cycle.

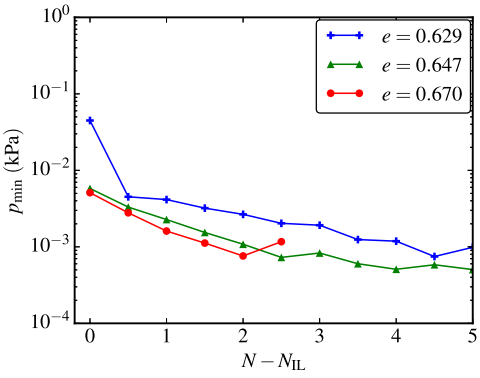

Fig. 4. Variation of the lowest pressure $p_{\min}$ reached in the post-liquefaction period against the number of cycles from initial liquefaction $N - N_{\text{IL}}$ for three samples with different void ratios all subjected to CSR = 0.25.

viscosity with increasing shear rate. To explore the effect of shear rate on the macroscopic response near the fluid-like to solid-like transition, we recorded from the post-liquefaction cycle C a state A soon after S_1 and then we sheared the dense sample for a range of different shear rates. The corresponding stress–strain response and stress ratio versus mean stress are presented in Fig. 5. A smaller shear rate induces a larger shear strain development in fluid-like state (between S_2 and S_3) and a lower $p_{\min}$. Near and after S_4 ($p \simeq 1$ kPa), the stress ratio τ/p levels off for the smaller shear rates but not for the highest rate. This implies that the system sheared for $v_x = 0.1$ m/s has not yet reached the typical butterfly shape at S_4 since its values are not yet steady (for a

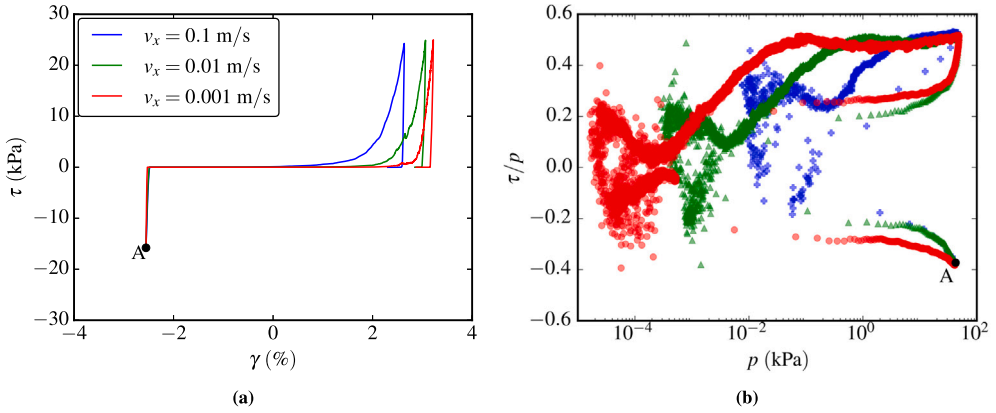

Fig. 5. Effect of shear rate on the (a) stress–strain response and (b) stress ratio versus mean stress in the first half of post-liquefaction cycle C.

unique value of τ/p preserved along the butterfly shape). Interestingly, the shear rate does not noticeably affect the saturated value of τ/p.

Generally, the granular system encompasses both solid-like and fluid-like features, either of which is dominant in a certain loading period. From the perspective of solid mechanics, the shear modulus G and dilatancy D are the most interesting properties. The shear modulus is defined as the ratio $\Delta\tau/\Delta\gamma$ of shear stress increment $\Delta\tau$ and shear strain increment $\Delta\gamma$. However, estimating dilatancy D is quite challenging and requires special techniques (e.g., Martin et al., 1975; Hu et al., 2020) in the constant-volume simulations, especially in the liquefaction state. It is defined as the plastic volumetric strain increment induced by a plastic shear strain increment:

$$D = \frac{\mathrm{d}\varepsilon_{\mathrm{v}}^{\mathrm{p}}}{|\,\mathrm{d}\gamma^{\mathrm{p}}|} = \frac{\mathrm{d}\varepsilon_{\mathrm{v}} - \mathrm{d}\varepsilon_{\mathrm{v}}^{\mathrm{e}}}{|\,\mathrm{d}\gamma - \mathrm{d}\gamma^{\mathrm{e}}|}, \tag{2}$$

where the superscripts p and e refer to plastic and elastic, respectively, and ε_{v} is the volumetric strain. Under the constant-volume condition ($\mathrm{d}\varepsilon_{\mathrm{v}} = 0$), we may neglect $\mathrm{d}\gamma^{\mathrm{e}}$, which is significantly smaller than plastic shear strain. Hence, the expression of D can be further simplified as

$$D = -\frac{\mathrm{d}\varepsilon_{\mathrm{v}}^{\mathrm{e}}}{|\,\mathrm{d}\gamma - \mathrm{d}\gamma^{\mathrm{e}}|} \simeq -\frac{\mathrm{d}\varepsilon_{\mathrm{v}}^{\mathrm{e}}}{|\,\mathrm{d}\gamma|} = -\frac{\mathrm{d}p}{K^{\mathrm{e}}|\,\mathrm{d}\gamma|} \tag{3}$$

where K^{e} is the elastic bulk modulus of the granular assembly. Previous studies based on the Hertz contact law (Agnolin and Roux, 2007; Khalili et al., 2017) suggest a power relation between K^{e} and p, i.e., $K^{\mathrm{e}} \propto p^n$, with the exponent n having a value between 0.33 and 0.4. In the case of the linear contact law, one expects $n = 0$, i.e., independence of pressure (Pouragha and Wan, 2018). But there is a dependence for large deformations due to new contacts gained as the pressure increases, i.e., a dependence on the contact density (the number of contacts per unit volume). Since the contact density does not change significantly, this dependence is neglected in estimating D. Thus one can deduce from Eq. (3) the following expression:

$$D \propto D' = \frac{\mathrm{d}p}{|\,\mathrm{d}\gamma|}. \tag{4}$$

The flow behavior can also be described in terms of effective shear and normal viscosities defined by $\eta_t = \tau/\dot{\gamma}$ and $\eta_n = \sigma_n/\dot{\gamma}$, respectively, where σ_n is the vertical effective stress. These effective viscosities are particularly relevant to the liquefied states and it is expected that they are small in the fluid-like states and increase in the solid-like states. The viscous and frictional points of view for the description of granular flows are equivalent as recently highlighted by both experiments and numerical simulations (Boyer et al., 2011; Amarsid et al., 2017), but they have never been used for liquefaction. The effective viscosities can be normalized by $\rho\bar{d}^2\dot{\gamma}$, which represents a reference viscosity defined from the natural physical quantities ρ, $\bar{d}$ and $\dot{\gamma}$ of the system (Amarsid et al., 2017):

$$c_t = \frac{\eta_t}{\rho\bar{d}^2\dot{\gamma}},\ c_n = \frac{\eta_n}{\rho\bar{d}^2\dot{\gamma}}. \tag{5}$$

The variations of G, D', c_t, and c_n against p are presented in Fig. 6, with cycle C highlighted with the same color codes as in Fig. 2. As expected, G decreases significantly when the sample liquifies ($p \leq 1$ kPa), corresponding to a fluid-like behavior. Compared with the values in non-liquefied region, D' also exhibits a diminishing trend when $p \leq 1$ kPa, except in the first part of reverse shearing (from S_1 to S_2 for example) presenting a large amount of contraction. The much smaller values of G and D' in the fluid-like region ($p \leq 1$ kPa) compared with those outside this region support the proposition of Barrero et al. (2020) to significantly reduce both plastic modulus and dilatancy for simulating liquefaction-induced shear strains.

Regarding the effective viscosities, we observe in Fig. 6(c) and (d) variations over more than five orders of magnitude. c_t is a linear function of p for $p > 0.1$ kPa in the loading scenario, where the behavior is solid-like. For $p < 0.1$ kPa, c_t falls off dramatically as p declines, and remains nearly constant in the fluid-like state. Unlike c_t, c_n always presents a strongly linear relation with p. The proportionality of c_t and c_n with p in the solid-like state is consistent with the numerical findings of Amarsid et al. (2017) and Vo et al. (2020). Indeed, dimensional analysis implies $c_t = \mu/I^2$ and $c_n = 1/I^2$ where $\mu = \tau/p$ is the apparent friction coefficient. While variations of μ can affect the relation between c_t and p, c_n mainly depends on p. For a given shear rate and large values of p, μ is nearly constant and equal to the critical-state value μ_c of the internal friction coefficient. Hence, $c_t \simeq \mu_c/I^2 \propto p$. Fig. 6(c) clearly shows that the effective granular shear viscosity can be used as a marker of transition between fluid-like and solid-like states.

The simulated data for different shear rates were observed to be different in Fig. 5(b). We find that the same data collapse well in the quasi-static range ($I < 10^{-3}$) when considered in the parametric space of c_t and I, as shown in Fig. 7. The black fitting line confirms a power-law relation between c_t and I, as discussed in the previous paragraph. They differ, however, for $I > 10^{-3}$ where increasingly higher values of I and lower values of c_t are reached as the shear rate increases, supporting thereby the shear-thinning nature of the flow in the fluid-like state.

4. Micro- and meso-scale response

We now consider two microscopic and two mesoscale quantities to represent the internal structure of the granular system, focusing on their evolutions prior to and after the transition between solid-like and fluid-like states in the post-liquefaction period. The two microscopic descriptors are the geometrical coordination number z_g and fabric anisotropy a_c. z_g is defined as the average number of contacts per particle excluding floaters (particles without contacts) (Thornton, 2015):

$$z_{\mathrm{g}} = \frac{2N_c}{N_p - N_p^0}, \tag{6}$$

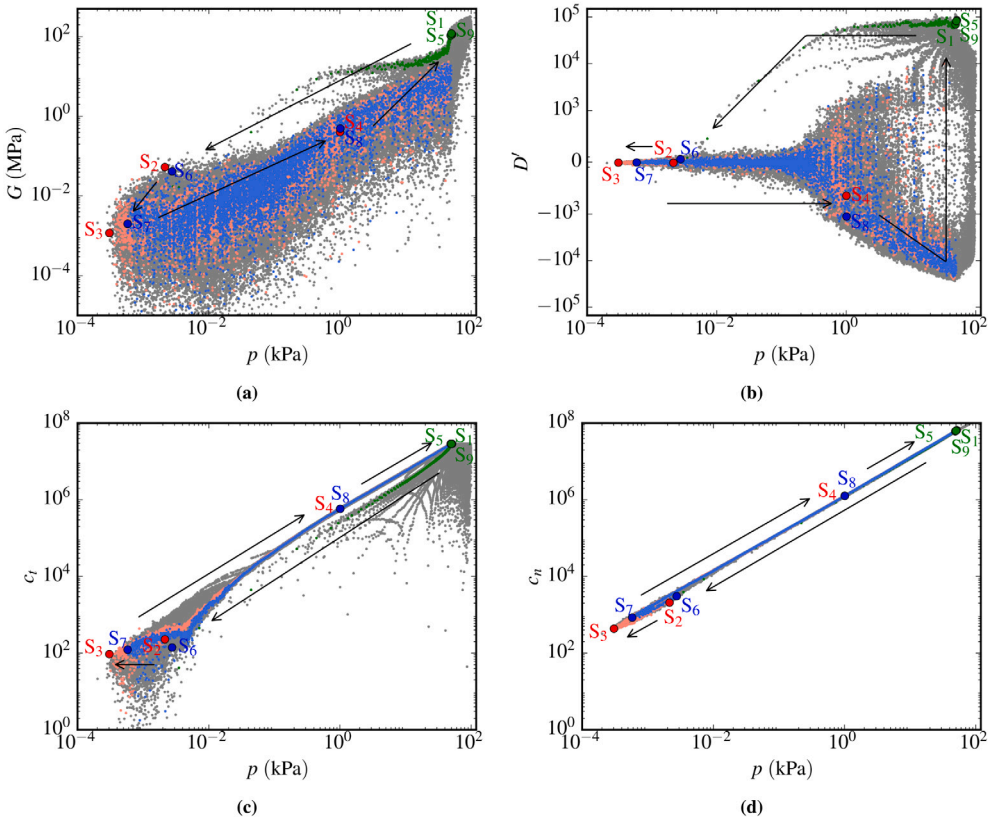

Fig. 6. Variations of (a) shear modulus $G \simeq \Delta\tau/\Delta\gamma$, (b) dilatancy $D \propto D' \simeq -\Delta p/|\Delta\gamma|$, (c) effective normalized shear viscosity c_t, and (d) effective normalized normal viscosity c_n based on shear strain increment $|\Delta\gamma| \simeq 0.001\%$ and $\dot{\gamma} = 0.38\ \mathrm{s}^{-1}$.

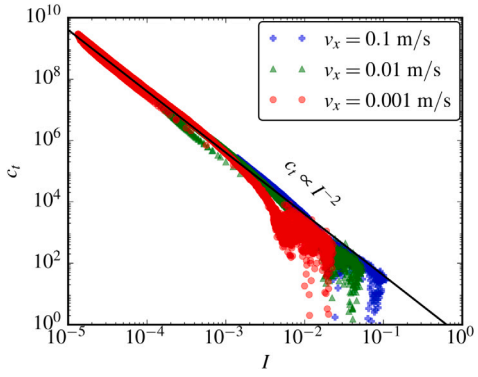

Fig. 7. Effect of shear rate on the relation between normalized shear viscosity c_t and inertial number I.

where N_p is the number of particles and N_p^0 is the number of floaters. z_g can approximate the level of static redundancy in the system, namely the difference between the total number of constraints and the total number of degrees of freedom. As we use a nonzero resistance to rolling and torsion at the contacts between particles, each contact contributes six constraints, i.e. three force components and three moments, which are the unknowns of the isostatic problem. The isostatic (Roux, 2000) coordination number based on $6N_c = 6(N_p - N_p^0)$, i.e., by equating the number of degrees of freedom and the number of constraints, implies $z_g = 2$ in our system (Yang et al., 2022b). To reveal the vectorial nature of the contact network, the deviatoric invariant of fabric anisotropy tensor was used to quantify the degree of geometrical anisotropy related to the directional distribution of contact normals $\boldsymbol{n}$, namely

$$a_c = \mathrm{sign}(S_c)\sqrt{\frac{3}{2}\boldsymbol{a}_c : \boldsymbol{a}_c}. \tag{7}$$

$\boldsymbol{a}_c$ is the fabric anisotropy tensor defined by

$$\boldsymbol{a}_c = \frac{15}{2}(\boldsymbol{\phi}_c - \frac{1}{3}\boldsymbol{I}), \tag{8}$$

where $\boldsymbol{I}$ is the second-order identity tensor and $\boldsymbol{\phi}_c$ is the fabric tensor related to $\boldsymbol{n}$ (Oda, 1982):

$$\boldsymbol{\phi}_c = \frac{1}{N_c}\sum_{c\in N_c} \boldsymbol{n}\otimes\boldsymbol{n}. \tag{9}$$

S_c is the normalized first joint invariant (Guo and Zhao, 2013) between the deviatoric stress tensor $\mathbf{s} = \boldsymbol{\sigma} - p\boldsymbol{I}$ and fabric anisotropy tensor $\boldsymbol{a}_c$, given by

$$S_c = \frac{\boldsymbol{a}_c : \mathbf{s}}{\sqrt{\boldsymbol{a}_c : \boldsymbol{a}_c}\sqrt{\mathbf{s} : \mathbf{s}}}. \tag{10}$$

Generally S_c quantifies the level of coaxiality between $\mathbf{s}$ and $\boldsymbol{a}_c$, with $S_c = 1.0$ corresponding to the case of proportionality.

The mesoscale quantities describe features pertaining to particle clusters. We define a k-cluster as a group of touching particles with their internal contacts bearing a normal force $f_n > k\langle f_n\rangle$, where $\langle f_n\rangle$ is the average normal force and k is a pre-defined force threshold. Thus, on one hand, one can come up with the number of k-clusters denoted as N_{cluster}, and the fraction of the maximum k-cluster size (Martin et al., 2020) with respect to the total number of particles, denoted as f_{MC}. On the other hand, one can compare the dimensions of the maximum k-cluster, namely force transmission network for $k > 0$, with the corresponding dimensions of the granular system, from which the percolation index is derived as ξ_i/L_i ($i = x,\ y,\ z$ in 3D) (Bi et al., 2011; Huang et al., 2019b). Here ξ_i and L_i refer to the dimensions of the largest k-cluster and the granular system along i-direction, respectively.

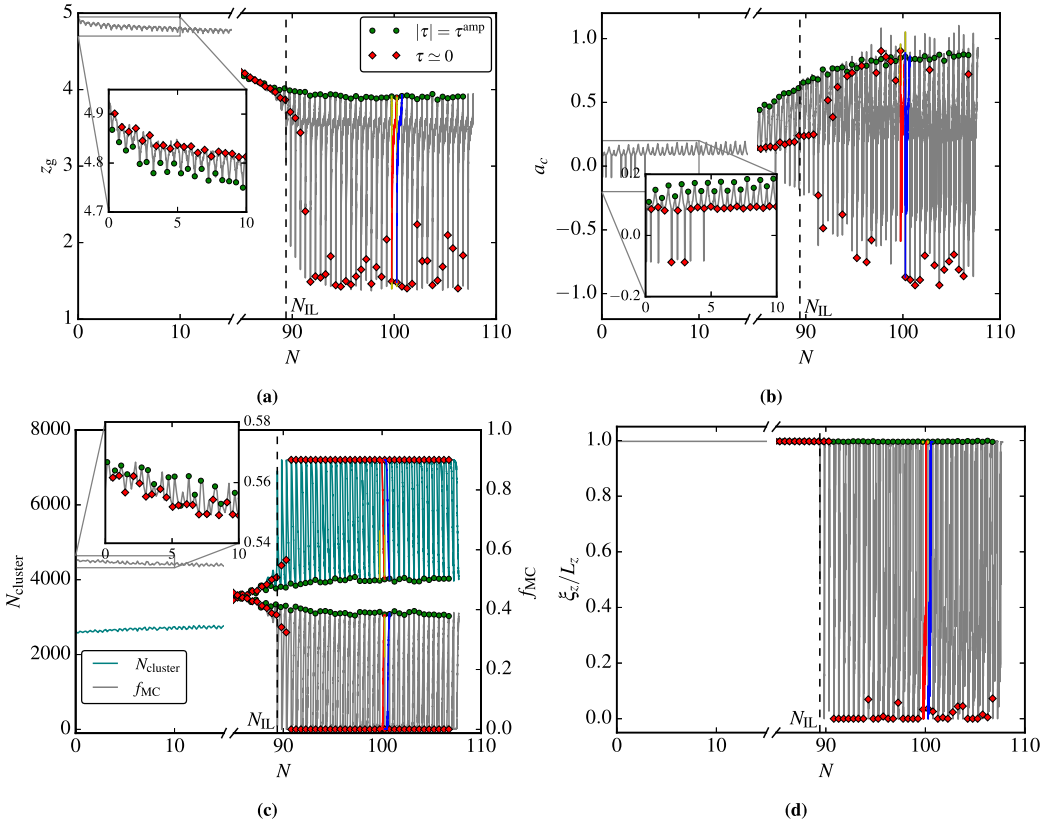

Fig. 8. Evolutions of micro- and meso-scale descriptors in the whole cyclic shearing period: (a) coordination number z_g; (b) fabric anisotropy a_c; (c) particle k-cluster with $k = 1$; (d) percolation index ξ_z/L_z with $k = 1$.

In the following, we set $k = 1$, namely the strong force transmission network (Radjai et al., 1998). Given the in-sync variations of the three percolation indices, only ξ_z/L_z is presented for simplicity.

Fig. 8 displays the evolutions of the four types of descriptors in the whole cyclic shearing process. The states of $|\tau| = \tau^{amp}$ and $\tau \simeq 0$ are highlighted by markers. According to the initial liquefaction (IL), namely the first time that r_u reaches the limit 0.99, the process is divided into pre- and post-liquefaction periods. All these quantities change mildly in the pre-liquefaction period and oscillate significantly in the post-liquefaction period due to the transition between solid-like and solid-like states. During the whole process, the solid-like state at $|\tau| = \tau^{amp}$ shows an overall decrease in z_g, an increase in a_c, a decrease in the number of clusters, and a decrease in the maximum cluster size with percolation index nearly unchanged and equal to 1. The liquefaction states associated with $\tau \simeq 0$ in the post-liquefaction period correspond to low values of z_g and percolation index, implying a fluid-like behavior.

Fig. 9 presents evolutions of these micro- and mesoscale quantities in the selected post-liquefaction cycle C of Fig. 2. Upon reverse loading from S_1 (or S_5) to S_2 (or S_6), a sudden drop in z_g is observed in Fig. 9(a), implying the collapse of the geometrical contact network. This is consistent with the rise in the number of clusters in Fig. 9(c) which indicates more isolated smaller particle clusters. The vanishing of f_{MC} and ξ_z/L_z in Figs. 9(c) and (d), respectively, further confirms the absence of a percolating strong force-transmitting network when the system initially falls into liquefaction. The computed value of a_c in Fig. 9(b) also oscillates significantly, indicating the out-of-sync (non-proportionality) between internal structure and external loading, meaning that the system is in a state that is unable to maintain a solid structure. Since the reverse loading induces the instability so rapidly, it is not reasonable to introduce critical values of micro and meso descriptors to characterize the solid-like to fluid-like transition.

Following the reverse loading after S_2 (or S_6), the liquefied granular system tends to reconstruct its contact network gradually. This process is featured by increasing z_g, oscillating but overall decreasing a_c (in absolute value), decreasing $N_{cluster}$, and increasing f_{MC}, as shown in Fig. 9. The phase transformation state (minimum p at S_3 or S_7) is not associated with the minimum of z_g, where the former lags behind the latter, contradicting the observations in some monotonic shearing studies of Barnett et al. (2020) and Rahman et al. (2021). This might be due to the collapsing contact network near these states where N_p^0/N_p noticeably affects the relation between p and z_g: $p \propto z_g(1 - N_p^0/N_p)\langle l f_n \rangle$ (Yang et al., 2021). As we shall see below, the minimum value of pressure corresponds to the isostatic value $z_g = 2$. A quick increase of z_g occurs from S_2, where z_g is below 2, to S_3, where $z_g = 2$. This increase of z_g despite a decrease of p indicates the complexity of nonlinear microstructural changes in the liquefaction state. The gain of contacts is accompanied by a change of sign of a_c (rotation of the fabric tensor) and its decrease in absolute value. This observation clearly shows that the isostatic coordination number plays a key role in cyclic shearing of granular materials.

Slightly after $\Theta = 90°$ or $\gamma = 0$, a_c, f_{MC}, and ξ_z/L_z present an increasing trend while $N_{cluster}$ decreases more rapidly. This signals the stable formation of interconnected network (Huang et al., 2019a) starting to propagate across the whole system. The practical criterion $r_u = 0.99$ to exit the fluid-like state (S_4 or S_8) corresponds to a local plateau of z_g ($\simeq 3.6$), where the largest force transmission network percolates across the granular system from both compressive and extensional directions, indicating a full regain of contact network. But Figs. 9(a) and (d) suggest that the fluid-like to solid-like transition happens earlier than S_4 or S_8, questioning the choice of $r_u = 0.99$. We will return to this issue later.

By comparing Figs. 9(a) and (d), one can observe certain correlation in the evolutions of z_g and ξ_z/L_z, especially near the transition between solid-like and fluid-like states. Fig. 10 presents ξ_z/L_z vs z_g in the cyclic

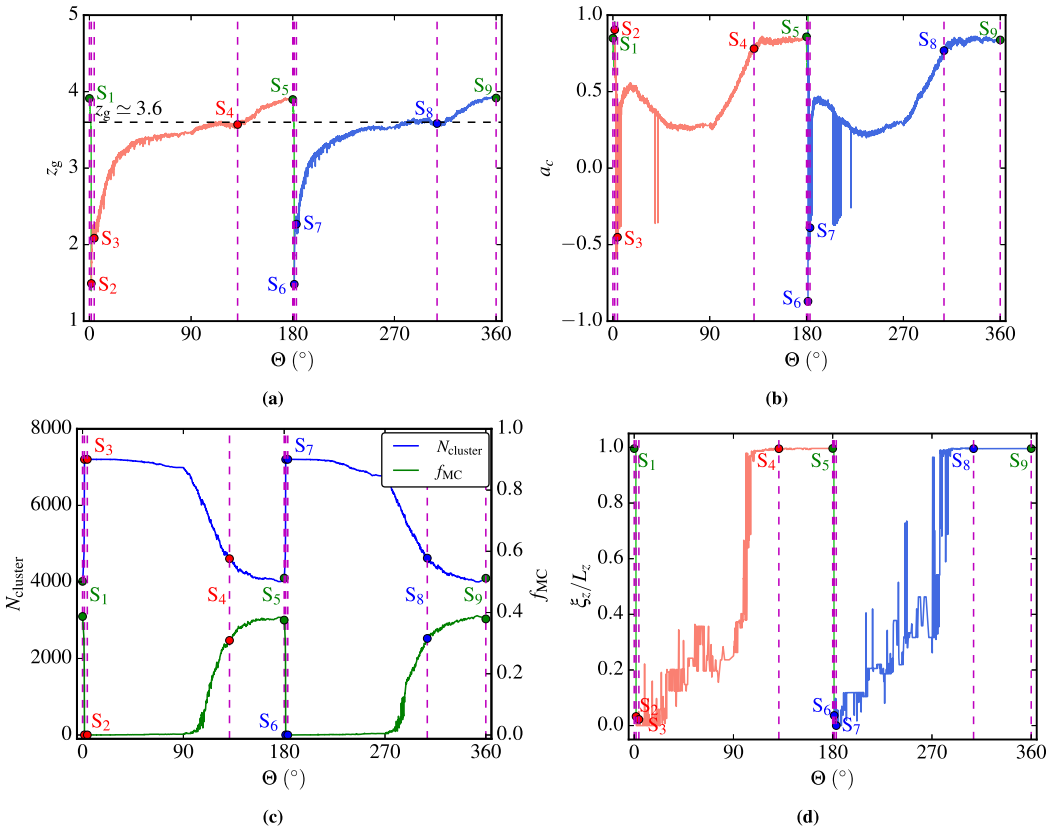

Fig. 9. Evolutions of micro- and meso-scale descriptors in the post-liquefaction cycle C: (a) coordination number z_g; (b) fabric anisotropy a_c; (c) particle k-cluster with $k = 1$; (d) percolation index ξ_z/L_z with $k = 1$.

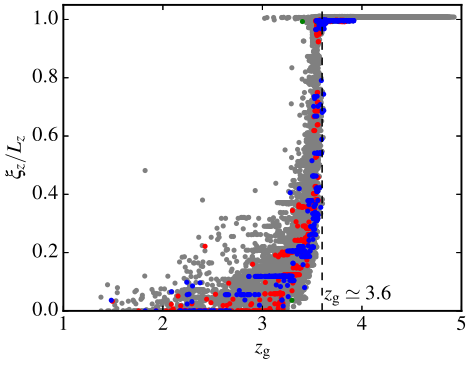

Fig. 10. Percolation index ξ_z/L_z with $k = 1$ versus coordination number z_g during the cyclic shearing (colored points come from the post-liquefaction cycle C).

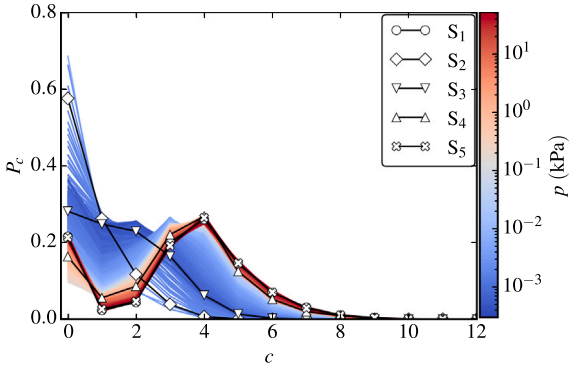

Fig. 11. Connectivity diagram expressing the fractions P_c of particles with exactly c contacts in the post-liquefaction cycle C.

shearing process. The coincidence between $z_g \simeq 3.6$ and abrupt jump of ξ_z/L_z to 1 confirms the claim that $z_g \simeq 3.6$ is the critical value for the percolation of the contact network across the granular system (Yang et al., 2021, 2022b). This allows the use of z_g as a simple criterion to judge whether the granular system is able to provide the geometrical contact network supporting significant force transmission.

Besides the aforementioned descriptors, Fig. 11 presents the particle connectivity diagram expressing the distribution of fractions P_c of particles with exactly c contacts, in the post-liquefaction cycle C. The states with higher levels of p (> 1 kPa), including S_1, S_4, and S_5, are associated with P_c distributions having the peak at $c = 4$ and longer tail for $c > 4$ – the common manifestation of a stable contact network. The onset of liquefaction (S_2) occurs with a sudden change in P_c distribution, exhibiting the highest proportion of floaters (lowest z_g). It represents the weakest state of the granular system. The continuous shearing brings the system to the collisional regime (near S_3) where the dynamic events such as binary collisions (P_1) and unstable chains (P_2) prevail. These events preclude particle clusters ($P_{c\geq 3}$) and the nucleation of the contact work.

5. Linking micro/meso to macro

In the last Section, we discussed the evolutions of micro and meso-scale descriptors during the fluid-like to solid-like transition, which present general agreement with the usual stress-based criterion for liquefaction. In this study, $r_u = 0.99$ corresponds to a mean stress threshold $p_{th} = 1$ kPa. Although the choice of p_{th} or r_u is arbitrary, it seems to work in many scenarios (Ishihara, 1993; Kokusho, 2013; Barrero et al., 2020; Yang et al., 2022a). Nevertheless, its micro- and meso-scale foundation needs to be clarified.

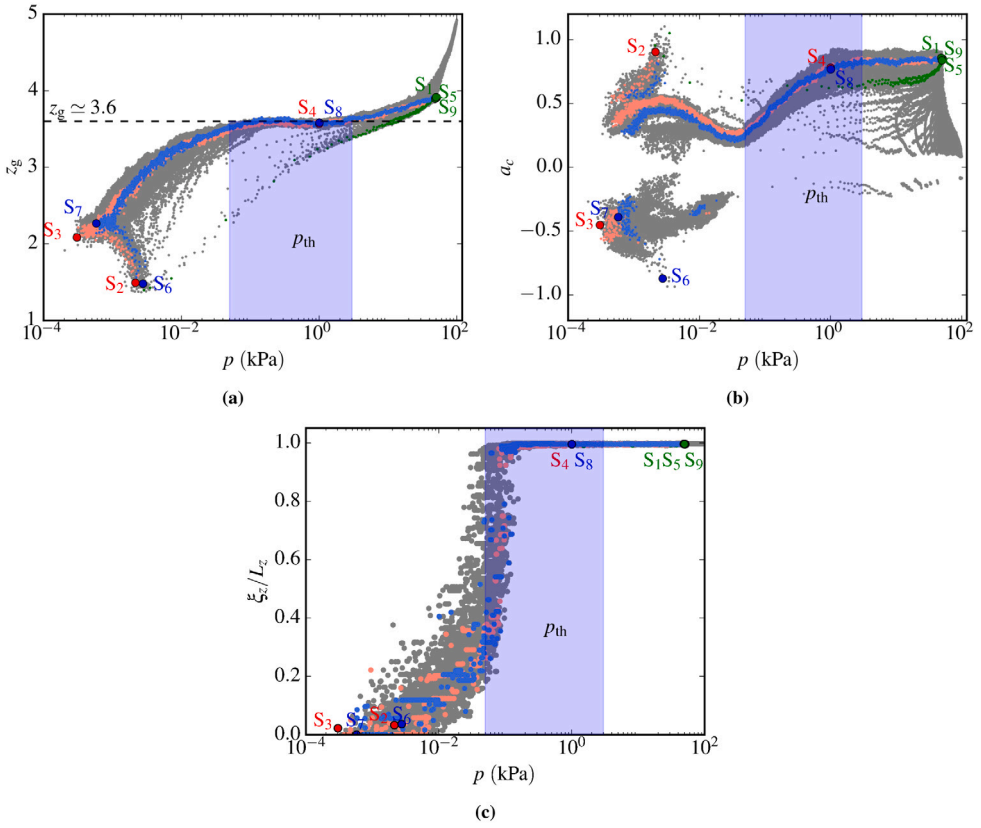

Fig. 12. Micro- and meso-scale descriptors versus mean stress during cyclic shearing: (a) coordination number z_g; (b) fabric anisotropy a_c; (c) percolation index ξ_z/L_z. p_{th} ranges between 0.05 and 3 kPa.

Fig. 12 shows the variations of micro and meso-scale descriptors including z_g, a_c, and ξ/L against the mean stress p during the whole cyclic shearing, with the post-liquefaction cycle C highlighted. In the post-liquefaction loading period from S_3 (or S_7) to S_5 (or S_9), Fig. 12(a) indicates a plateau of z_g when p ranges between 0.1 and 3 kPa. In the beginning of this range, the values of both $z_g \simeq 3.6$ and $\xi/L \simeq 1$ reveal that the contact network is fully rebuilt. But we do not know whether the internal structure is aligned with the external loading. The inset of stress path of Fig. 2(a) shows a constant shear stress ratio τ/p when p evolves from 0.05 kPa. At the same time, we observe an evolving positive a_c in Fig. 12(b). These observations contain two implications. The first implication is that the fabric tensor $\boldsymbol{a}_c$ and deviatoric stress tensor $\mathbf{s}$ are coaxial since a_c is positive. The second implication is that the internal structure is not fully organized to follow the external loading since a_c is not yet saturated. In this range, the number of contacts increases in the compressive direction but declines in the extensional direction to maintain a nearly constant z_g and an increasing a_c, the so-called 'anisotropic gain/loss of contacts' (Yang et al., 2021). When the system exits this range and the stress path evolves along the butterfly shape, one can see that a_c does not change noticeably along the loading and z_g increases slightly, implying that the number of contacts increases in both compressive and extensional directions, corresponding to isotropic gain of contacts.

The evolution of the micro and meso-scale variables suggest two options for the definition of p_{th}. If one cares about the thorough percolation of the contact network, the first instance of $\xi/L \simeq 1$ suggests $p_{th} \simeq 0.1$ kPa. If one considers the full alignment (proportionality) of internal structure with the external loading, then the first time a_c gets saturated we have $p_{th} \simeq 3$ kPa. Both choices of p_{th} are associated with the same value of z_g.

Table 2 summarizes the micro/meso/macro-scale meanings of the particular states in a post-liquefaction cycle. While the phase transformation state (S_3 and S_7) is clearly defined as the transition from compression to dilation, the corresponding microscale descriptors z_g and a_c take special values. z_g reaches its isostatic value (for the lowest pressure) and a_c takes a value between 0.4 and 0.5.; see Figs. 9(a) and (b). This value of anisotropy is the average anisotropy $\langle a_c \rangle = (z_{max} - z_{min})/(z_{max} + z_{min})$ of a system in which z_g oscillates between z_{min} and z_{max} (Radjai et al., 2012). The observed limits in the liquefaction state are $z_{min} \simeq 1.5$ and $z_{max} \simeq 4$, yielding $\langle a_c \rangle \simeq 0.45$.

Table 2
Summary of the meanings of the selected particular states in the post-liquefaction cycle C.

State ID	Micro	Meso	Macro
S_1, S_5 & S_9	Highest z_g & a_c	$\xi_z/L_z \simeq 1$	$\lvert\tau\rvert = \tau^{amp}$
S_2 & S_6	Lowest z_g	$\xi_z/L_z \simeq 0$	τ changing its sign
S_3 & S_7	Isostatic z_g	$\xi_z/L_z \simeq 0$	Lowest p
S_4 & S_8	$z_g \simeq 3.6$	$\xi_z/L_z \simeq 1$	$r_u \simeq 0.99$

6. Conclusion

In this study, we performed 3D-DEM constant-volume cyclic simple shear simulations to investigate the cyclic liquefaction of granular materials. The simulated macroscopic response shows general agreement with experiments. The initial solid-like granular system becomes fluid-like after a few loading cycles. The transition from solid-like to fluid-like behavior corresponds to sudden collapse of the load-bearing contact network happens rapidly. In contrast, the transition from fluid-like to solid-like behavior takes place during a long process of rebuilding of the contact network and was more specifically at the focus of this paper. For that we selected a typical post-liquefaction cycle and identified several particular states that divide the cycle into distinct periods. Once the granular system liquefies as a result of shear reversal, it goes through a short period featured by low shear modulus,

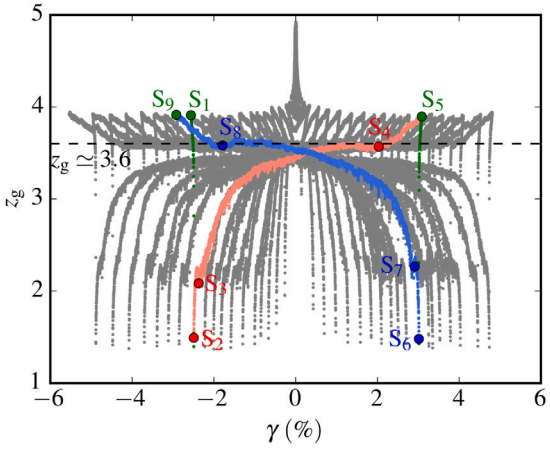

Fig. 13. Coordination number versus shear strain during cyclic shearing.

decreasing dilatancy, and reduced shear viscosity. The majority of fluid-like shear strain develops during the dilation period. Our simulations do not show null mean effective stress in liquefaction state for loose and dense samples.

We analyzed the internal structure evolution during the whole shearing process by means of several micro- and mesoscale descriptors: the coordination number, the fabric anisotropy, the number of strong stress-transmitting clusters, the fraction of maximum cluster size, and a percolation index defined from the extension of the largest cluster. The onset of liquefaction is accompanied by low coordination number, large oscillations of fabric anisotropy, increasing number of particle clusters, and vanishing of the largest force-transmitting network. Along with shear deformation, the contact network is gradually rebuilt through a sequence of binary collisions and nucleation of particle clusters. The fluid-like to solid-like transition, i.e., exiting the fluid-like state, is characterized by the well-defined value 3.6 of the coordination number and by the percolation index equal to 1. During this transition, the fabric anisotropy tends to align with external loading. Another key observation was that the lowest values of the coordination number are not reached at the phase transformation point where the lowest pressure is reached. Instead, we observe that upon shear stress sign change in the liquefaction state the coordination number undergoes a sudden increase to its isostatic value with pressure having its lowest value. The sudden decrease of anisotropy in the same process is clearly a consequence of the gain of contacts along the direction of extensional deformation as a result of shear stress sign change. After this fast change of the microstructure, a longer period of contact network rebuilt is observed during which most of shear strain is developed.

These findings can be used to improve stress-based criteria in continuum models of cyclic liquefaction. Moreover, micromechanical models can also be developed by using microscale variables such as coordination number and fabric anisotropy as internal variables. In this case, it will be important to clearly distinguish the short-time effect of shear stress sign change, resulting in a nearly discontinuous increase of the coordination number, from the more progressive rebuilding of the contact network. Furthermore, the accumulation of shear strain in successive cycles reveals a memory effect that was not discussed in this paper. For instance, Fig. 13 shows the evolution of the coordination number as a function of the cumulative shear strain. We see that there is no apparent evolution of the specific values of the coordination number despite the observed increasing shear strain with successive cycles. The memory of the granular configuration may well be hidden in more subtle variables at the mesoscopic scale, e.g. the size and distribution of clusters. Some trends can be observed in Fig. 8, but a more detailed investigation is necessary in the future.

CRediT authorship contribution statement

Ming Yang: Conceptualization, Methodology, Software, Formal analysis, Investigation, Writing – review & editing, Visualization. **Mahdi Taiebat:** Conceptualization, Methodology, Investigation, Resources, Writing – review & editing, Supervision, Project administration, Funding acquisition. **Farhang Radjaï:** Conceptualization, Methodology, Investigation, Writing – review & editing.

Declaration of competing interest

The authors declare that they have no known competing financial interests or personal relationships that could have appeared to influence the work reported in this paper.

Acknowledgments

Financial support for this study was provided by the Natural Sciences and Engineering Research Council of Canada (NSERC).

References

Agnolin, I., Roux, J.-N., 2007. Internal states of model isotropic granular packings. III. Elastic properties. Phys. Rev. E 76 (6), 061304. http://dx.doi.org/10.1103/PhysRevE.76.061304.

Amarsid, L., Delenne, J.-Y., Mutabaruka, P., Monerie, Y., Perales, F., Radjai, F., 2017. Viscoinertial regime of immersed granular flows. Phys. Rev. E 96 (1), 012901. http://dx.doi.org/10.1103/PhysRevE.96.012901.

Barnett, N., Rahman, M.M., Karim, M.R., Nguyen, H.B.K., 2020. Evaluating the particle rolling effect on the characteristic features of granular material under the critical state soil mechanics framework. Granul. Matter 22 (4), 1–24. http://dx.doi.org/10.1007/s10035-020-01055-5.

Barrero, A.R., Oquendo, W., Taiebat, M., Lizcano, A., 2018. Cyclic shearing response of granular material in the semi-fluidized regime. In: Geotechnical Earthquake Engineering and Soil Dynamics V: Numerical Modeling and Soil Structure Interaction. pp. 100–107. http://dx.doi.org/10.1061/9780784481479.010.

Barrero, A.R., Taiebat, M., Dafalias, Y.F., 2020. Modeling cyclic shearing of sands in the semifluidized state. Int. J. Numer. Anal. Methods Geomech. 44 (3), 371–388. http://dx.doi.org/10.1002/nag.3007.

Bi, D., Zhang, J., Chakraborty, B., Behringer, R.P., 2011. Jamming by shear. Nature 480 (7377), 355–358. http://dx.doi.org/10.1038/nature10667.

Boyer, F., Guazzelli, E., Pouliquen, O., 2011. Unifying suspension and granular rheology. Phys. Rev. Lett. 107 (18), 188301. http://dx.doi.org/10.1103/PhysRevLett.107.188301.

Castro, G., 1975. Liquefaction and cyclic mobility of saturated sands. J. Soil Mech. Found. Div. 101 (GT6), 551–569. http://dx.doi.org/10.1061/ajgeb6.0000173.

Chen, Y., Liu, H., Wu, H., 2013. Laboratory study on flow characteristics of liquefied and post-liquefied sand. Eur. J. Environ. Civ. Eng. 17 (S1), s23–s32. http://dx.doi.org/10.1080/19648189.2013.834583.

Chen, G., Zhou, E., Wang, Z., Wang, B., Li, X., 2016. Experimental investigation on fluid characteristics of medium dense saturated fine sand in pre-and post-liquefaction. Bull. Earthq. Eng. 14 (8), 2185–2212. http://dx.doi.org/10.1007/s10518-016-9907-6.

Cundall, P.A., Strack, O.D.L., 1979. A discrete numerical model for granular assemblies. GÉOtechnique 29 (1), 47–65. http://dx.doi.org/10.1680/geot.1979.29.1.47.

Dafalias, Y.F., Manzari, M.T., 2004. Simple plasticity sand model accounting for fabric change effects. J. Eng. Mech. 130 (6), 622–634. http://dx.doi.org/10.1061/(ASCE)0733-9399(2004)130:6(622).

Elgamal, A., Yang, Z., Parra, E., Ragheb, A., 2003. Modeling of cyclic mobility in saturated cohesionless soils. Int. J. Plast. 19 (6), 883–905. http://dx.doi.org/10.1016/S0749-6419(02)00010-4.

Fardad Amini, P., Huang, D., Wang, G., Jin, F., 2021. Effects of strain history and induced anisotropy on reliquefaction resistance of Toyoura sand. J. Geotech. Geoenviron. Eng. 147 (9), 04021094. http://dx.doi.org/10.1061/(ASCE)GT.1943-5606.0002588.

Gu, X., Zhang, J., Huang, X., 2020. DEM analysis of monotonic and cyclic behaviors of sand based on critical state soil mechanics framework. Comput. Geotech. 128, 103787. http://dx.doi.org/10.1016/j.compgeo.2020.103787.

Guo, N., Zhao, J., 2013. The signature of shear-induced anisotropy in granular media. Comput. Geotech. 47, 1–15. http://dx.doi.org/10.1016/j.compgeo.2012.07.002.

Heussinger, C., Barrat, J.-L., 2009. Jamming transition as probed by quasistatic shear flow. Phys. Rev. Lett. 102 (21), 218303. http://dx.doi.org/10.1103/PhysRevLett.102.218303.

Hu, Q., Zhang, J.-M., Wang, R., 2020. Quantification of dilatancy during undrained cyclic loading and liquefaction. Comput. Geotech. 128, 103853. http://dx.doi.org/10.1016/j.compgeo.2020.103853.

Huang, X., Hanley, K.J., Zhang, Z., Kwok, C.-y., 2019a. Structural degradation of sands during cyclic liquefaction: Insight from DEM simulations. Comput. Geotech. 114, 103139. http://dx.doi.org/10.1016/j.compgeo.2019.103139.

Huang, X., Hanley, K.J., Zhang, Z., Kwok, C.-y., Xu, M., 2019b. Jamming analysis on the behaviours of liquefied sand and virgin sand T subject to monotonic undrained shearing. Comput. Geotech. 112, 112–125. http://dx.doi.org/10.1016/j.compgeo.2019.03.008.

Huang, X., Kwok, C.-y., Hanley, K.J., Zhang, Z., 2018. DEM analysis of the onset of flow deformation of sands: linking monotonic and cyclic undrained behaviours. Acta Geotech. 13 (5), 1061–1074. http://dx.doi.org/10.1007/s11440-018-0664-3.

Hwang, J.-I., Kim, C.-Y., Chung, C.-K., Kim, M.-M., 2006. Viscous fluid characteristics of liquefied soils and behavior of piles subjected to flow of liquefied soils. Soil Dyn. Earthq. Eng. 26 (2–4), 313–323. http://dx.doi.org/10.1016/j.soildyn.2005.02.020.

Ishihara, K., 1993. Liquefaction and flow failure during earthquakes. GÉOtechnique 43 (3), 351–451. http://dx.doi.org/10.1680/geot.1993.43.3.351.

Ishihara, K., Tatsuoka, F., Yasuda, S., 1975. Undrained deformation and liquefaction of sand under cyclic stresses. Soils Found. 15 (1), 29–44. http://dx.doi.org/10.3208/sandf1972.15.29.

Khalili, M.H., Roux, J.-N., Pereira, J.-M., Brisard, S., Bornert, M., 2017. Numerical study of one-dimensional compression of granular materials. II. Elastic moduli, stresses, and microstructure. Phys. Rev. E 95 (3), 032908. http://dx.doi.org/10.1103/PhysRevE.95.032908.

Kokusho, T., 2013. Liquefaction potential evaluations: energy-based method versus stress-based method. Can. Geotech. J. 50 (10), 1088–1099. http://dx.doi.org/10.1139/cgj-2012-0456.

Kuhn, M.R., Renken, H.E., Mixsell, A.D., Kramer, S.L., 2014. Investigation of cyclic liquefaction with discrete element simulations. J. Geotech. Geoenviron. Eng. 140 (12), 04014075. http://dx.doi.org/10.1061/(asce)gt.1943-5606.0001181.

Liao, D., Yang, Z.X., 2021. Hypoplastic modeling of anisotropic sand behavior accounting for fabric evolution under monotonic and cyclic loading. Acta Geotech. 16, 2003–2029. http://dx.doi.org/10.1007/s11440-020-01127-z.

Martin, G.R., Seed, H.B., Finn, W.L., 1975. Fundamentals of liquefaction under cyclic loading. J. Geotech. Eng. Div. 101 (5), 423–438. http://dx.doi.org/10.1061/AJGEB6.0000164.

Martin, E.L., Thornton, C., Utili, S., 2020. Micromechanical investigation of liquefaction of granular media by cyclic 3D DEM tests. GÉOtechnique 70 (10), 906–915. http://dx.doi.org/10.1680/jgeot.18.p.267.

MiDi, G.D.R., 2004. On dense granular flows. Eur. Phys. J. E 14 (4), 341–365. http://dx.doi.org/10.1140/epje/i2003-10153-0.

Mitchell, J.K., Soga, K., et al., 2005. Fundamentals of Soil Behavior, vol. 3. John Wiley & Sons New York.

Mutabaruka, P., 2013. Numerical Modeling of Immersed Granular Media: Initiation and Propagation of Avalanches in a Fluid (Ph.D. thesis). Université Montpellier II-Science and Technology of Languedoc, Montpellier, France.

Mutabaruka, P., Taiebat, M., Pellenq, R.J.-M., Radjai, F., 2019. Effects of size polydispersity on random close-packed configurations of spherical particles. Phys. Rev. E 100 (4), 042906. http://dx.doi.org/10.1103/PhysRevE.100.042906.

Ng, T.-T., Dobry, R., 1994. Numerical simulations of monotonic and cyclic loading of granular soil. J. Geotech. Eng. 120 (2), 388–403. http://dx.doi.org/10.1061/(ASCE)0733-9410(1994)120:2(388).

Ni, X., Ye, B., Zhang, F., Feng, X., 2021. Influence of specimen preparation on the liquefaction behaviors of sand and its mesoscopic explanation. J. Geotech. Geoenviron. Eng. 147 (2), 04020161. http://dx.doi.org/10.1061/(asce)gt.1943-5606.0002456.

Oda, M., 1982. Fabric tensor for discontinuous geological materials. Soils Found. 22 (4), 96–108. http://dx.doi.org/10.3208/sandf1972.22.4_96.

Papadimitriou, A.G., Bouckovalas, G.D., Dafalias, Y.F., 2001. Plasticity model for sand under small and large cyclic strains. J. Geotech. Geoenviron. Eng. 127 (11), 973–983. http://dx.doi.org/10.1061/(ASCE)1090-0241(2001)127:11(973).

Pouragha, M., Wan, R., 2018. On elastic deformations and decomposition of strain in granular media. Int. J. Solids Struct. 138, 97–108. http://dx.doi.org/10.1016/j.ijsolstr.2018.01.002.

Radjai, F., Delenne, J.-Y., Azéma, E., Roux, S., 2012. Fabric evolution and accessible geometrical states in granular materials. Granul. Matter http://dx.doi.org/10.1007/s10035-012-0321-8.

Radjaï, F., Dubois, F., 2011. Discrete-Element Modeling of Granular Materials. Wiley-Iste.

Radjaï, F., Roux, J.-N., Daouadji, A., 2017. Modeling granular materials: century-long research across scales. J. Eng. Mech. 143, 04017002. http://dx.doi.org/10.1061/(ASCE)EM.1943-7889.0001196.

Radjai, F., Wolf, D.E., Jean, M., Moreau, J., 1998. Bimodal character of stress transmission in granular packings. Phys. Rev. Lett. 80, 61–64. http://dx.doi.org/10.1103/PhysRevLett.80.61.

Rahman, M.M., Nguyen, H.B.K., Fourie, A.B., Kuhn, M.R., 2021. Critical state soil mechanics for cyclic liquefaction and postliquefaction behavior: DEM study. J. Geotech. Geoenviron. Eng. 147 (2), 04020166. http://dx.doi.org/10.1061/(asce)gt.1943-5606.0002453.

Roux, J.-N., 2000. Geometric origin of mechanical properties of granular materials. Phys. Rev. E 61 (6), 6802. http://dx.doi.org/10.1103/PhysRevE.61.6802.

Shamoto, Y., Zhang, J.-M., Goto, S., 1997. Mechanism of large post-liquefaction deformation in saturated sand. Soils Found. 37 (2), 71–80. http://dx.doi.org/10.3208/sandf.37.2_71.

Sitharam, T.G., 2003. Discrete element modelling of cyclic behaviour of granular materials. Geotech. Geol. Eng. 21 (4), 297–329. http://dx.doi.org/10.1023/B:GEGE.0000006036.00597.0b.

Tasiopoulou, P., Gerolymos, N., 2016. Constitutive modeling of sand: Formulation of a new plasticity approach. Soil Dyn. Earthq. Eng. 82, 205–221. http://dx.doi.org/10.1016/j.soildyn.2015.12.014.

Thornton, C., 2015. Granular Dynamics, Contact Mechanics and Particle System Simulations. Springer.

Vaid, Y.P., Sivathayalan, S., 1996. Static and cyclic liquefaction potential of Fraser Delta sand in simple shear and triaxial tests. Can. Geotech. J. 33 (2), 281–289. http://dx.doi.org/10.1139/t96-007.

Vargas, R.R., Ueda, K., Uemura, K., 2020. Influence of the relative density and K0 effects in the cyclic response of Ottawa F-65 sand-cyclic Torsional Hollow-Cylinder shear tests for LEAP-ASIA-2019. Soil Dyn. Earthq. Eng. 133, 106111. http://dx.doi.org/10.1016/j.soildyn.2020.106111.

Vo, T.T., Nezamabadi, S., Mutabaruka, P., Delenne, J.-Y., Radjai, F., 2020. Additive rheology of complex granular flows. Nature Commun. 11 (1), 1–8. http://dx.doi.org/10.1038/s41467-020-15263-3.

Wang, G., Wei, J., 2016. Microstructure evolution of granular soils in cyclic mobility and post-liquefaction process. Granul. Matter 18 (3), 51. http://dx.doi.org/10.1007/s10035-016-0621-5.

Wang, R., Zhang, J.-M., Wang, G., 2014. A unified plasticity model for large post-liquefaction shear deformation of sand. Comput. Geotech. 59, 54–66. http://dx.doi.org/10.1016/j.compgeo.2014.02.008.

Wei, J., Huang, D., Wang, G., 2018. Microscale descriptors for particle-void distribution and jamming transition in pre- and post-liquefaction of granular soils. J. Eng. Mech. 144 (8), 04018067. http://dx.doi.org/10.1061/(ASCE)EM.1943-7889.0001482.

Wu, J., Kammerer, A.M., Riemer, M.F., Seed, R.B., Pestana, J.M., 2004. Laboratory study of liquefaction triggering criteria. In: 13th World Conference on Earthquake Engineering. (2580), p. 14.

Yamada, S., Takamori, T., Sato, K., 2010. Effects on reliquefaction resistance produced by changes in anisotropy during liquefaction. Soils Found. 50 (1), 9–25. http://dx.doi.org/10.3208/sandf.50.9.

Yang, J., Sze, H.Y., 2011. Cyclic behaviour and resistance of saturated sand under non-symmetrical loading conditions. GÉOtechnique 61 (1), 59–73. http://dx.doi.org/10.1680/geot.9.P.019.

Yang, M., Taiebat, M., Dafalias, Y.F., 2022a. SANISAND-MSf: a sand plasticity model with memory surface and semifluidised state. GÉOtechnique 72 (3), 227–246. http://dx.doi.org/10.1680/jgeot.19.p.363.

Yang, M., Taiebat, M., Mutabaruka, P., Radjaï, F., 2021. Evolution of granular materials under isochoric cyclic simple shearing. Phys. Rev. E 103, 032904. http://dx.doi.org/10.1103/PhysRevE.103.032904.

Yang, M., Taiebat, M., Mutabaruka, P., Radjaï, F., 2022b. Evolution of granular media under constant-volume multidirectional cyclic shearing. Acta Geotech. 17, 779–802. http://dx.doi.org/10.1007/s11440-021-01239-0.

Zhang, J.-M., Wang, G., 2012. Large post-liquefaction deformation of sand, part I: physical mechanism, constitutive description and numerical algorithm. Acta Geotech. 2 (7), 69–113. http://dx.doi.org/10.1007/s11440-011-0150-7.